Biosensors and Bioelectronics 177 (2021) 112966

Contents lists available at ScienceDirect

Biosensors and Bioelectronics

journal homepage: http://www.elsevier.com/locate/bios

Short communication

Anomalous sensitivity enhancement of nano-graphitic electrochemical micro-sensors with reducing the operating voltage

Edoardo Cuniberto [a], Abdullah Alharbi [a,b], Zhujun Huang [a], Ting Wu [c], Roozbeh Kiani [c,d], Davood Shahrjerdi [a,e,*]

[a] Electrical and Computer Engineering, New York University, Brooklyn, NY, 11201, USA
[b] National Center for Nanotechnology and Semiconductors, KACST, Riyadh, 12354, Saudi Arabia
[c] Center for Neural Science, New York University, New York, NY, 10003, USA
[d] Department of Psychology, New York University, New York, NY, 10003, USA
[e] Center for Quantum Phenomena, Physics Department, New York University, New York, NY, 10003, USA

ARTICLE INFO

Keywords:
Sensitivity
Electrochemical sensor
Graphitic carbon
Voltammetry sensing

ABSTRACT

Microscopic interactions between electrochemical sensors and biomolecules critically influence the sensitivity. Here, we report an unexpected dependence of the sensitivity on the upper potential limit (UPL) in voltammetry experiments. In particular, we find that the sensitivity of substrate-supported nano-graphitic micro-sensors in response to dopamine increases almost linearly with the inverse of UPL in voltammetry experiments with rapid potential sweeps. Our experiments and multi-physics simulations reveal that the main cause behind this phenomenon is the UPL-induced electrostatic force that influences the steady-state number of dopamine molecules on the sensor surface. Our findings illustrate a new strategy for enhancing the performance of planar electrochemical micro-sensors.

1. Introduction

Over thirty years of continuous progress has established carbon-based electrochemical micro-sensors as a useful tool for monitoring fast neurotransmission activities in the brain (Huffman and Venton 2009; Millar et al., 1985; Rodeberg et al., 2017; Venton and Cao 2020). The small geometric dimension (micron size) of existing sensors has been the key to spatially-resolved monitoring of chemical signaling in the nervous system. It has also been a critical factor for increasing the temporal resolution by allowing the application of rapid potential sweep (RPS) waveforms in electrochemical voltammetry measurements (Bard and Faulkner 2001; Wightman 1981). However, existing carbon micro-sensors have limited sensitivity (i.e., the amount of current generated due to the redox reactions in the presence of unit concentration of the molecule), which is adequate mostly for the detection of large modulations of dopamine release in deep brain structures (Day et al., 2007; Hart et al., 2014; Rodeberg et al., 2017; Sugam et al., 2012). Enhancing the sensitivity of carbon micro-sensors is essential for detecting smaller releases.

Therefore, a significant research focus has been on exploring various carbon nanomaterials for building highly sensitive micro-sensors (Cao et al., 2019; Cuniberto et al., 2020; Demuru et al., 2018; Puthongkham and Venton 2019; Schmidt et al., 2013). A common research theme on this topic has been to incorporate a substantial amount of structural defects in candidate carbon nanomaterials. The rationale for this material optimization strategy is the favorable effect of defects on increasing the electron transfer (Bowling et al., 1989; Rice and McCreery 1989; Zhong et al., 2014), which is a fundamental physical process that controls the sensitivity (Cuniberto et al., 2020; Wu et al., 2019; Zhu 2017). Due to their nanoscale dimensions, it is possible to incorporate many defects in a given area within the sensor surface, where the electrochemical reactions occur. However, this approach has an upper physical limit. For example, the electron transfer rate, hence the sensitivity, in graphitic materials degrades when the spatial density of defects exceeds a threshold, coinciding with the transition of the graphitic material into a fully disordered carbon (Wu et al., 2019; Zhong et al., 2014). Therefore, defect engineering approaches must be complemented with additional means for further enhancement of the sensitivity.

In voltammetry with an RPS waveform, the sensitivity is proportional to the number of adsorbed molecules on the sensor surface (Bard

* Corresponding author. Electrical and Computer Engineering, New York University, Brooklyn, NY, 11201, USA.
E-mail address: davood@nyu.edu (D. Shahrjerdi).

https://doi.org/10.1016/j.bios.2021.112966
Received 14 September 2020; Received in revised form 13 December 2020; Accepted 31 December 2020
Available online 5 January 2021

and Faulkner 2001). Hence, increasing the number of adsorbed molecules has been used as another means for enhancing the sensitivity. One way to achieve this has been to incorporate a hold time between the measurement cycles of the RPS waveform (Bath et al., 2000; Venton and Cao 2020). While increasing the hold time increases the sensitivity, it diminishes the temporal resolution of the sensing measurements—which is an undesirable outcome. Past research has also found that using a more negative potential during the hold time can enhance the adsorption of positively charged molecules, such as dopamine, through electrostatic attraction (Heien et al., 2003; Venton and Cao 2020). The use of negatively charged polymeric coatings (e.g., Nafion) has been another way of boosting the electrostatic attraction of positively charged molecules to the sensor surface (Gerhardt et al., 1984; Vreeland et al., 2015). These findings of the past studies indicate the significance of discovering new ways for boosting the sensitivity by increasing the number of surface molecules.

Here, we report an anomalous increase in the sensitivity of substrate-supported micro-sensors made of nano-graphitic (NG) carbon by decreasing the positive upper potential limit (UPL) of the RPS waveform. In contrast, we observe that the amplitude of the charging current of the sensors is insensitive to UPL. We find that these observations are universal among our NG micro-sensors containing different amounts of structural defects. We use these advantageous features of NG micro-sensors for *in vitro* measurements of dopamine with concentrations as low as 10 nM. Lastly, we establish, through experiments and multi-physics simulations, that the UPL-induced electrostatic interactions between the NG micro-sensor and dopamine molecules play a significant role in enhancing the sensitivity.

2. Material and methods

2.1. Fabrication of substrate-supported NG micro-sensors

We have reported the details of the fabrication process in a previous study (Cuniberto et al., 2020). In brief, NG carbon islands were formed directly on silicon substrates covered with SiO_2 through a nickel-induced graphitization process (see Supplementary Information for details). The NG carbon islands were then made into functional devices by making high-quality Cr/Au metal contacts using a combination of electron-beam lithography (EBL), metal deposition in an electron-beam evaporator, and metal lift-off. Lastly, a protection layer was formed through EBL patterning of an SU8 film.

2.2. NG carbon characterization

We characterized the NG carbon using atomic force microscopy (AFM; Bruker Dimension FastScan), x-ray photoelectron spectroscopy (XPS; Physical Electronics Versaprobe II), and transmission electron microscopy (TEM; FEI Titan Themis 200).

2.3. Electrochemical measurements

Cyclic voltammetry measurements were performed using both N-shaped and triangular potential waveforms with a potential sweep rate (ν) of 200 V/s and a repetition rate of 10 Hz. A custom-made Y-shaped microfluidic chamber, combined with two syringe pumps (World Precision Instruments) were used to deliver 1× phosphate buffered saline (PBS) solution (Sambrook et al., 1989) and dopamine in PBS solution during the measurements. A chlorinated silver wire (Ag/AgCl) was used as the reference electrode.

For measurements of low-concentration dopamine, we used a custom-made integrated circuit (IC) (You et al., 2020). The data acquisition and analysis for this read-out system were performed with a custom-made user interface program developed in MATLAB. We also show that the low-concentration detection of dopamine using NG micro-sensors is feasible using electronic boards made of commercial off-the-shelf (COTS) components (Supplementary Fig. S4).

For the voltage-dependent measurements and the time-evolution measurements, the current was recorded using a low-noise current amplifier (SR570, Stanford Research Systems) together with a data acquisition instrument (NI USB-6363 series, National Instruments). This readout setup was controlled with a custom-made LabVIEW control interface.

2.4. Chemicals

Dopamine hydrochloride powder was first dissolved in 1× PBS to a stock concentration of 2 mM. Dopamine solutions with the desired known concentrations were then prepared by diluting the stock solution in 1× PBS. The 1× PBS (pH of 7.4) was prepared by dissolving 8 g of sodium chloride, 1.44 g of sodium phosphate dibasic, 240 mg of potassium phosphate monobasic, and 200 mg potassium chloride in 1 L of de-ionized water. All chemicals were purchased from Sigma Aldrich.

3. Results and discussions

3.1. Observation of UPL dependence of dopamine sensitivity

In cyclic voltammetry with an RPS waveform, the resulting redox current is typically plotted against the waveform potential. This plot, known as the cyclic voltammogram, allows the identification of an analyte from the location of the redox peak potentials and the determination of the analyte concentration from the amplitude of the redox currents. Therefore, the lower and upper potential limits (i.e., LPL and UPL) of the waveform should be chosen such that the voltammogram displays the full shapes of the oxidation and reduction current peaks due to a target analyte. To fulfill this condition, as we show later, the minimum required potential range can be relatively small. Therefore, an important question arises when adjusting the RPS waveform for a sensing experiment: Is there a benefit in pushing the potential beyond the minimum range required for constructing the cyclic voltammogram?

We studied the above question using substrate-supported micro-sensors made of NG carbon in RPS measurements of dopamine. Fig. 1a–c shows the side-view illustration and representative top-view optical images of NG micro-sensors. We made these sensors directly on SiO_2-covered silicon substrates using standard nano-fabrication techniques (Cuniberto et al., 2020). The NG micro-sensors have a relatively smooth surface topography (generally a root mean square, RMS, surface roughness of 10 nm or less), as shown in Fig. 1d. We have also quantitatively analyzed the atomic composition and chemistry of the sensor surface using the XPS (see Supplementary Information for details). We made two main observations from the representative XPS data in Fig. 1e. First, the sensor surface consists of sp^2-hybridized C–C bonds, evident from both the position and the asymmetry of the C 1s peak (Berman et al., 2016, Biesinger). This observation is consistent with the fully capacitive nature of the background current (shown later). Second, there is no observable evidence of Ni catalyst on the sensor surface. Our TEM studies, shown in Fig. 1f, indicate the preferential (but not perfect) directionality of the graphitic planes within the film. Further, we found that Ni catalyst accumulates near the bottom of the NG carbon film, consistent with the absence of Ni from the XPS data.

After the device fabrication, the sensor sample was placed inside a custom-made microfluidic chamber, as shown in Fig. 1b. This setup allows a sequential flow of PBS and dopamine solutions while applying the RPS waveform and recording the current output of the micro-sensors.

We started the experiments by studying how the change of UPL influences the amplitude of the background charging current (I_{bg}) and the sensitivity to dopamine. We used two triangular waveforms with UPL of 1.15 V and 0.6 V, while keeping the LPL (−0.4 V) and the potential sweep rate (ν = 200 V/s) fixed, as shown in Fig. 2a. Fig. 2b shows that varying UPL has no observable influence on the background characteristics of the micro-sensor in terms of both the shape and amplitude.

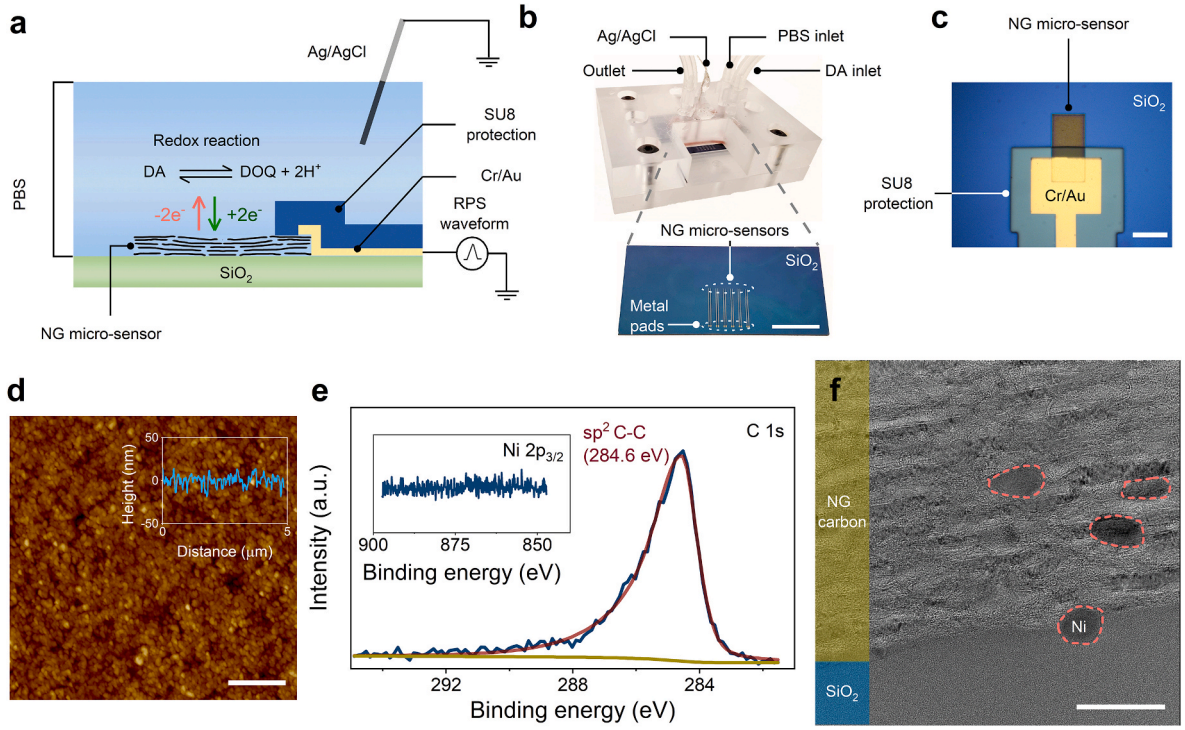

Fig. 1. Experimental set-up and NG carbon characterization. a) Cross-sectional schematic of the experimental set up used for the RPS measurements of dopamine (DA). **b)** Picture of the custom-made micro-fluidic chamber used in the experiment together with a representative optical image of a sensor sample, consisting of multiple planar NG micro-sensors. The scale bar is 1 cm. **c)** A close-up optical image of an individual NG micro-sensor. The scale bar is 25 μm. **d).** An example of a topographic AFM image of an NG micro-sensor (RMS roughness: ~8 nm). The inset shows a line scan. The scale bar is 1 μm. **e).** XPS analysis indicates the graphitic nature of the sensor surface, evident from the C–C bond peak highlighted in red. The Blue curve is the collected XPS data and the yellow is the background. The inset shows the detailed scan for the primary XPS region of Ni, indicating no detectable Ni catalyst on the sensor surface. **f)** Cross-sectional TEM image of NG carbon grown on SiO_2. The Ni clusters are marked with dashed red lines. The scale bar is 50 nm. (For interpretation of the references to colour in this figure legend, the reader is referred to the Web version of this article.)

A dopamine solution with a known concentration of 500 nM was introduced after the PBS flow, while continuously recording the output current of the micro-sensor. The cyclic voltammogram, shown in Fig. 2c, was then constructed by subtracting the output current measured in the dopamine solution from the background current recorded in PBS. The data indicate that a UPL as low as 0.6 V is adequate for resolving the full shape of the dopamine oxidation current. However, and surprisingly, we observed about a factor of two increase in the peak of the oxidation current ($I_{ox,peak}$) by decreasing the UPL from 1.15 V to 0.6 V. From this plot, we also found that the other key characteristics of the oxidation and reduction current peaks, including the full-width at half-maximum (FWHM) and the location of the peaks, were almost unchanged. We note that this observation is independent of the geometry of the micro-fluidic chamber (see Supplementary Information Fig. S3). Also, as we show later, these effects of UPL are generalizable to our NG micro-sensors. The noticeable increase of $I_{ox,peak}$ by decreasing UPL contrasts with the characteristics of free-standing carbon micro-sensors, for which the sensitivity has no apparent dependence on UPL (Heien et al., 2003; Venton and Cao 2020).

Having observed the significant effect of UPL, we then studied how varying LPL (i.e., the potential during the hold time in a triangular waveform) influences the response of the NG micro-sensor to dopamine. We did so by applying triangular waveforms with varying LPL values of −0.2 V and −0.4 V, while fixing UPL at 0.6 V and ν at 200 V/s. Interestingly, we observed that decreasing the LPL has a negligible effect on $I_{ox,peak}$, as shown in Fig. 2d. The effect of LPL on the peak amplitude of the reduction current ($I_{red,peak}$) was also small (only about 15%). The LPL-dependence characteristic of the substrate-supported NG micro-sensors contrasts with the free-standing carbon micro-sensors (Venton and Cao 2020), for which the use of a more negative potential during the hold time is beneficial for increasing the sensitivity.

Enhancing the sensitivity is beneficial for improving the lowest detectable dopamine concentration. However, confounding factors (i.e., interferents) could prevent the reliable detection of dopamine at low concentrations. Among the various sources of interference are the variations of the current generated by the quinone-like species (marked in Fig. 2b with blue shading and labeled as $I_{quinone}$). An example of the interference by $I_{quinone}$ is the general observation of a small feature (typically < 1 nA) as a shoulder in the oxidation current peak of dopamine when using a triangular waveform in our *in vitro* experiments. We have marked this feature with an arrow in Fig. 2d. This feature is also commonly observed in RPS measurements of dopamine with a triangular waveform using other types of carbon micro-sensors (e.g., see Refs (Dengler and McCarty 2013; Schmidt et al., 2013)). More broadly, the variations of $I_{quinone}$ could be significant when there is a noticeable change in the local pH levels (Runnels et al., 1999; Takmakov et al., 2010). The removal of features due to the $I_{quinone}$ variation from the voltammogram is critical for a reliable detection of dopamine at low concentrations.

An optimal solution for minimizing the interference by $I_{quinone}$ is to reduce its amplitude significantly. We did so by engineering an N-shaped waveform with a small hold potential of −50 mV, as shown in Fig. 2e. Fig. 2f shows the background characteristics of the NG micro-sensor in response to the N-shaped waveform, indicating a significant reduction of $I_{quinone}$. Further, the background current characteristics remain nearly unchanged with varying UPL, similar to the experiments using the triangular waveform.

We then performed *in vitro* sensing experiments using the N-shaped waveform with a varying UPL of 1.15 V and 0.6 V. Fig. 2g shows the cyclic voltammograms, which we obtained for dopamine with a known

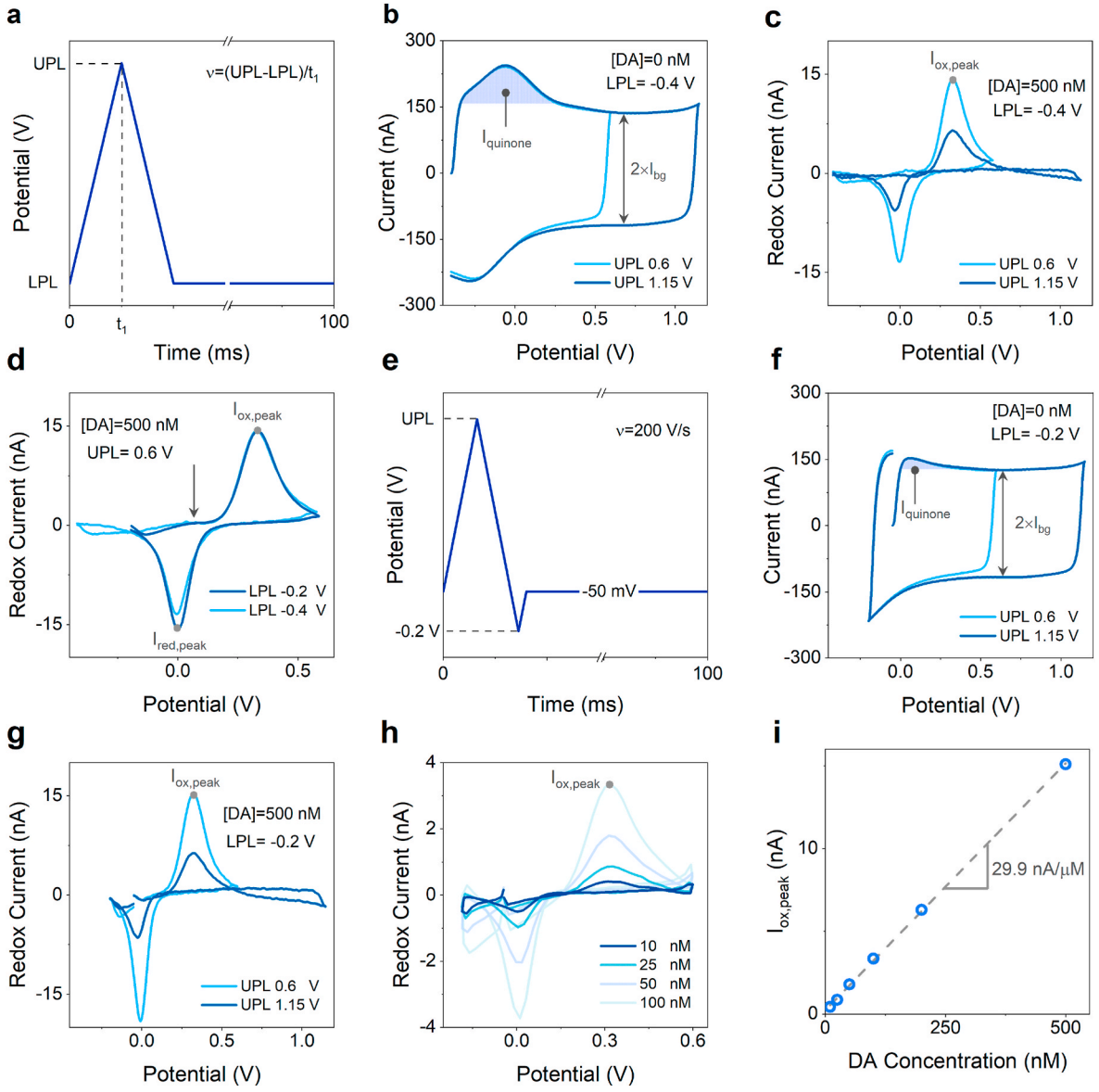

Fig. 2. Effect of LPL and UPL on sensor characteristics. a) A single-cycle schematic of a triangular RPS waveform used commonly in dopamine sensing experiments. **b)** Background charging current measured at two different UPL values of 0.6 V and 1.15 V. $I_{quinone}$ indicates the interfering current from quinone-like species in the solution. **c)** The corresponding dopamine cyclic voltammograms, indicating about two times increase in sensitivity with decreasing UPL. **d)** Varying LPL from −0.4 V to −0.2 V had no observable effect on $I_{ox,peak}$. Notice the shoulder, marked with an arrow. **e)** Schematic of the N-shape RPS waveform with LPL = −0.2 V, UPL = +0.6 V, and a hold potential of −50 mV. **f)** The background charging current measured using the N-shape waveform with UPLs of 0.6 V and 1.15 V. Notice the significant reduction of $I_{quinone}$. **g)** The corresponding dopamine cyclic voltammogram shows an increase of $I_{ox,peak}$ with reducing UPL, similar to the measurement in panel (c). **h)** The measured cyclic voltammogram of dopamine with concentrations as low as 10 nM. **i)** The calibration curve showing the linearity of the NG micro-sensor sensitivity. The linear fit to the data gives a sensitivity of 29.9 nA/μM.

concentration of 500 nM. Like the experiments using the triangular waveform, we observed about a factor of two increase in $I_{ox,peak}$ by decreasing UPL from 1.15 V to 0.6 V. Further, $I_{ox,peak}$ of the N-shaped and triangular waveforms with an identical UPL are nearly the same due to the negligible effect of the hold potential on $I_{ox,peak}$. However, the small shoulder due to $I_{quinone}$ interference is no longer visible in the cyclic voltammogram of dopamine. These characteristics of the N-shaped waveform allowed us to reliably resolve the cyclic voltammogram of low-concentration dopamine using the standard procedure for constructing the cyclic voltammogram (i.e., performing only background subtraction). In Fig. 2h, we show examples of voltammograms measured for several known concentrations of dopamine as low as 10 nM (see additional examples for another NG sensor in Supplementary Fig. S4). Fig. 2i shows the corresponding calibration curve of dopamine, which we measured for the physiological range of interest. The linear fit to the data confirms the well-behaved characteristics (i.e., linearity; see Supplementary Fig. S5) of the NG micro-sensor.

The above N-shaped waveform engineering for the detection of dopamine is a direct consequence of the disparate voltage dependence characteristics of our NG micro-sensors. This waveform engineering is, however, inaccessible to the existing carbon micro-sensors because they require a triangular waveform for achieving an optimal sensitivity performance.

3.2. *Experimental understanding of the UPL effect*

Our experiments established the strong dependence of the sensitivity of NG micro-sensors on UPL in voltammetry measurements using an RPS

waveform. We also demonstrated the immediate benefit of this phenomenon by measuring low concentrations of dopamine. However, revealing the physics behind this phenomenon is a critical next step, which could guide the development of new strategies for further enhancement of the sensitivity.

Two factors are the major contributors to the RPS sensitivity of the NG micro-sensors: the structural defects in NG carbon and the number of dopamine molecules on the sensor surface. We ruled out the effect of structural defects in the NG carbon as a cause for the observed increase of the sensitivity with decreasing UPL. Two observations provide strong evidence for this conclusion. The background current amplitude is proportional with the electrical double-layer capacitance, which depends strongly on the structural properties of the graphitic material (Chen et al., 2016; Hirunsit et al., 2016; Ji et al., 2014; Pak et al., 2014). However, the background current remained unchanged with varying UPL (e.g., see Fig. 2b). Moreover, the structural defects influence the electron transfer (Bowling et al., 1989; Rice and McCreery 1989; Zhong et al., 2014). The change in the electron transfer can be assessed qualitatively from the separation between the location of the peak oxidation and reduction currents (i.e., the potentials at which $I_{ox,peak}$ and $I_{red,peak}$

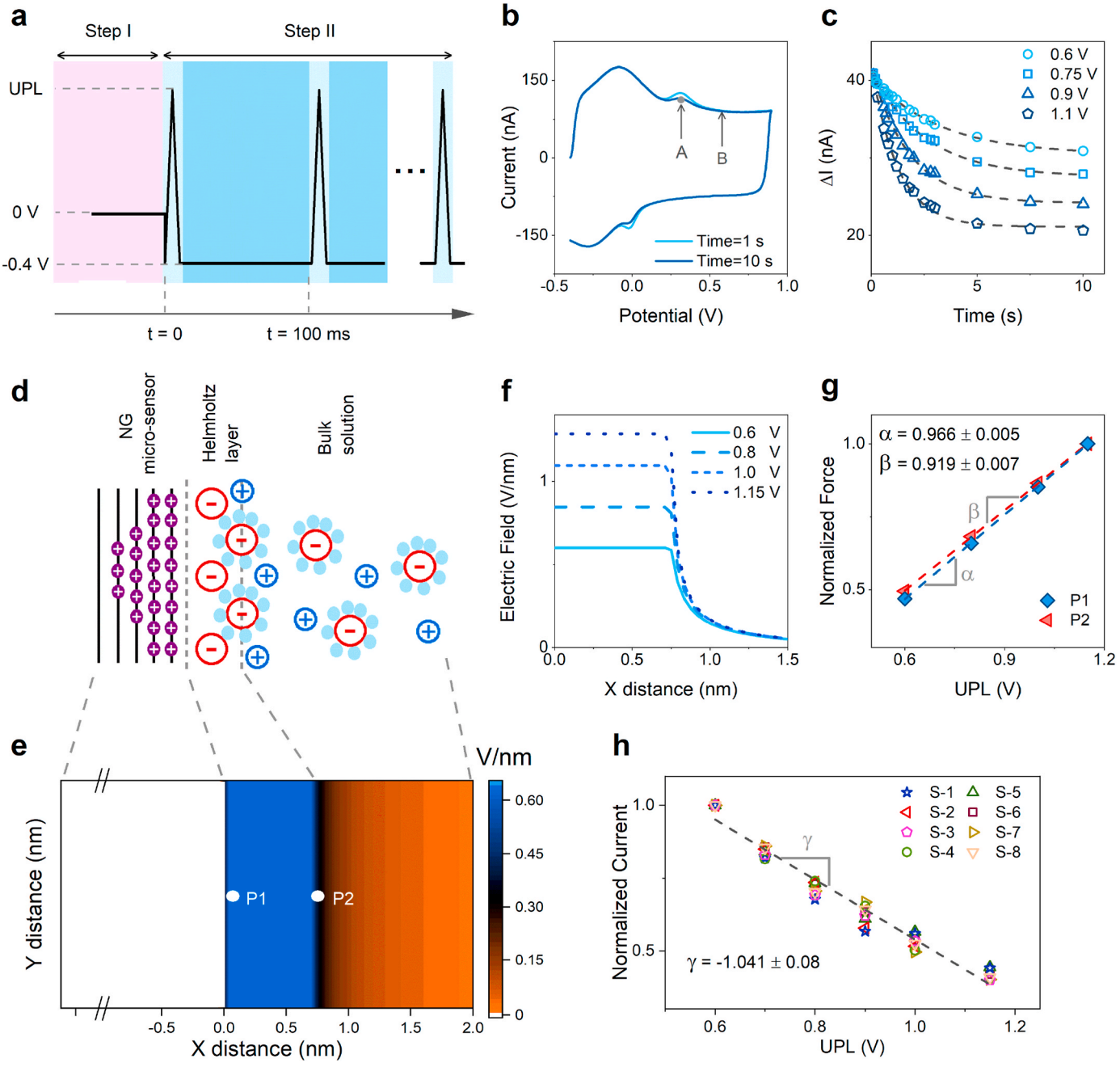

Fig. 3. Effect of UPL-induced electrostatic force on sensitivity. a) Conceptual representation of the two-step experiment that we used to study the time evolution of the peak oxidation current. **b)** Two example curves for measurements with UPL = 0.9 V, showing the total currents after 1 and 10 s. "A" and "B" indicate the potentials at which we obtained the current for calculating ΔI. **c)** The plot showing the time evolution of ΔI for four different UPL. The dashed lines are the exponential fits to the measured data points. **d)** Schematic of the structure used for the multi-physics simulations. **e)** Two-dimensional electric field map for UPL = 0.6 V, obtained from COMSOL simulations. **f)** Electric field profiles along the X distance for different UPLs. **g)** Normalized electrostatic force plotted against UPL at points "P1" and "P2". α and β are the slopes of the linear fits. **h)** Normalized $I_{ox,peak}$ plotted against UPL for multiple NG micro-sensors. The slope of the linear fit (γ) is consistent with the simulation results in panel (g).

occur) as well as the amplitude ratio of these two peak currents (Bard and Faulkner 2001; Schmidt et al., 2013). From the data in Fig. 2c, it is evident that these characteristics are nearly the same for different UPLs.

Therefore, we attribute the UPL-induced increase of the sensitivity to the increase in the steady-state number of dopamine molecules on the sensor surface. We hypothesized that, since dopamine molecules are positively charged at the physiological pH, due to the protonation of the amine side chain (Berfield et al., 1999; Jodko-Piorecka and Litwinienko 2013), the electrostatic force induced by the positive UPL has a significant role in establishing the steady-state equilibrium number of molecules on the NG micro-sensors.

We tested our hypothesis first by performing a new experiment that gives information on how the number of dopamine molecules participating in the redox reaction evolves in time by varying UPL. Fig. 3a illustrates the details of the experiment, which we repeated for four different UPL values while keeping the other parameters the same. Each experiment had two main steps. The first step (marked with purple shading in Fig. 3a) was designed to establish an initial equilibrium surface concentration of dopamine that is nearly the same for all measurements. We did so by filling the microfluidic chamber with a 1 μM dopamine solution and then holding the bias at 0 V on the NG micro-sensor for an additional 1 min. This design ensures that dopamine molecules have enough time to reach the sensor surface through free diffusion. This step was followed immediately by recording the sensor output in response to a triangular waveform. Each cycle of the waveform had two parts: (1) the potential ramps during which the redox reactions occur (marked with light blue shading in Fig. 3a), and (2) the hold time during which the dopamine surface concentration is replenished (marked with dark blue shading in Fig. 3a). Each cycle was repeated every 100 ms and the output current of the micro-sensor was recorded for 10 s.

Fig. 3b shows two example curves from the experiment with UPL = 0.9 V, which were recorded at times 1 s and 10 s. Interestingly, the data show the reduction of the peak of the oxidation current with time. To gain insight into how $I_{ox,peak}$ evolves in time, we analyzed the dataset for each UPL. For this analysis, we defined a new parameter, ΔI, which is the difference between the maximum of the apparent oxidation current peak (i.e., point "A" in Fig. 3b) and the current at the end of the apparent peak (i.e., point "B" in Fig. 3b). Tracking the changes of ΔI in time provides a good proxy for the time evolution of $I_{ox,peak}$ because the background characteristics of the NG micro-sensor is unchanged with UPL.

Fig. 3c shows the summary plot for the time evolution of ΔI for the measurements with UPLs of 0.6 V–1.1 V. We made three main observations from this plot. First, ΔI is decreasing over time for a given waveform. This observation indicates that prolonged and continued exposure to a waveform decreases the number of adsorbed molecules until a steady-state equilibrium is reached.

The decay of ΔI for each waveform is exponential with time. We verified this by making an exponential fit to each dataset in Fig. 3c using:

$$\Delta I(t) = \alpha e^{\frac{-t}{\tau}} + \beta$$

Table 1 gives the summary of the fitting parameters and the quality of the fit for each dataset. Interestingly, the time constant of the decay (τ) decreases with increasing UPL, suggesting that the effect of the mechanism behind the ΔI decay becomes stronger with higher UPL.

The second observation, confirmed by our curve fitting, is that the initial ΔI (i.e., at t = 0 s) is nearly the same for all measurements. This result confirms that the initial equilibrium concentration of dopamine for all measurements was nearly the same. Lastly, the steady-state equilibrium of ΔI shows an apparent dependence on UPL. The nearly equal spacing between the adjacent curves at t = 10 s indicates that the rate of change in the steady-state number of molecules is almost linear with the rate of UPL change. This observation agrees with our hypothesis, in that applying a larger UPL induces a larger repulsion force, hence pushing away more molecules at every measuring cycle until the equilibrium condition is reached. This experiment established the significant effect of UPL on the steady-state equilibrium number of molecules on the sensor surface during the RPS measurements.

Table 1
Exponential fit parameters of ΔI.

UPL (V)	α (nA)	β (nA)	τ (s)	ΔI(t = 0) (nA)	R^2
0.6	10.1 ± 0.13	30.5 ± 0.14	3.21 ± 0.11	40.6 ± 0.27	0.998
0.75	13.7 ± 0.2	27.6 ± 0.19	2.53 ± 0.09	41.3 ± 0.39	0.997
0.9	17.3 ± 0.2	24.1 ± 0.16	1.82 ± 0.05	41.4 ± 0.36	0.998
1.1	21.1 ± 0.22	21.1 ± 0.32	1.24 ± 0.05	42.2 ± 0.54	0.997

3.3. Multi-physics simulations of UPL-induced electrostatic force

Next, we used multi-physics numerical simulations to test our hypothesis on whether the UPL-induced electrostatic force can predict the observed dependence of $I_{ox,peak}$ on UPL. Fig. 3d shows the illustration of the structure that we used for our numerical simulations in COMSOL. The structure includes a 10 nm thick multi-layer graphene, a 0.75 nm thick Helmholtz layer, and a bulk ionic solution emulating the 1× PBS. We estimated the thickness of the Helmholtz layer by calculating the Debye length of the ionic solution (Section S3 in Supplementary Information), which agrees well with the previously calculated Debye length in 1× PBS (Chu et al., 2017; Mu et al., 2015; Narang et al., 2017; Villanueva et al., 2018). We simplified our simulations further by applying a constant UPL to multi-layer graphene. This setting represents a snapshot in time during the RPS measurements, when the sensor-molecule system has reached its steady-state equilibrium (see Fig. 3c). From the simulations, we obtained the two-dimensional distribution of the electrostatic field within the structure for a given UPL, as shown in Fig. 3e. We repeated these simulations for four different UPL values and plotted their corresponding electric field distributions along the length of the structure (Fig. 3f).

The next step is to estimate the electrostatic force acting on the dopamine molecules, which can be obtained from the product of the molecule charge and the electric field. Past research has established that the redox reactions of dopamine occur through a self-catalysis process, that is, dopamine molecules are adsorbed on the sensor surface and act as electro-catalyst for the electrochemical reaction (Bath et al., 2000; DuVall Stacy Hunt and McCreery 1999; DuVall Stacy H and McCreery 2000). Therefore, in our calculations we assumed that the dopamine molecules are on the NG carbon surface. The dopamine molecules (even in the solvated form) have a small dimension. As a result, it is reasonable to expect that the positive charge of the dopamine molecule will be located within the Helmholtz layer. Since the electric field within the Helmholtz layer is constant (Dubey and Guruviah 2019), we evaluated the normalized electrostatic force acting on the dopamine molecules from the electric field at the boundaries of the Helmholtz layer (i.e., points "P1" and "P2" in Fig. 3e). Fig. 3g shows the summary of the normalized force plotted against UPL at "P1" and "P2". The normalization was done relative to the force at UPL = 1.15 V. Interestingly, but not surprisingly, the repulsive force acting on dopamine molecules increases with UPL. The slopes of the linear fits to the data (denoted as α and β in the plot) quantify the rate of change in electrostatic force due to UPL.

Next, we examined whether the above simulation results can predict the experimental observations. Hence, we plotted the normalized $I_{ox,peak}$ against UPL, which we obtained experimentally for multiple NG micro-sensors, as shown in Fig. 3h (see Supplementary Fig. S2 for the background characteristics and voltammogram of each sensor device). The normalization for each micro-sensor was done relative to its $I_{ox,peak}$ at UPL = 0.6 V. The data indicate that the UPL-induced enhancement of sensitivity is universal to the NG micro-sensors, particularly since the sensors in this plot are from different samples that were produced at different fabrication runs. Moreover, a linear fit to the normalized $I_{ox,peak}$ data gives a slope (γ in Fig. 3h) that is consistent with the slope of the

linear fits to the normalized electrostatic force (i.e., α and β). These findings establish that the UPL-induced electrostatic interactions between the NG micro-sensor and dopamine molecules is the primary cause in changing the number of molecules participating in the redox reaction during RPS measurements.

4. Conclusions

We reported a new observation that reducing UPL in RPS measurements of dopamine using NG micro-sensors increases the sensitivity without changing the amplitude of the charging current. Our experiments and simulations establish that this phenomenon is due to the change in the number of surface molecules by the UPL-induced electrostatic force. Since this technique deals with the number of surface molecules, it is complementary to approaches that boost the electrochemical performance of the sensor through engineering its material structure (Cuniberto et al., 2020; Schmidt et al., 2013; Wu et al., 2019; Yang et al., 2016; Zhu 2017). By combining these two approaches, our NG micro-sensors achieve a sensitivity to background charging current (S–B) ratio as high as 0.35 nA $.\mu M^{-1}.nA^{-1}$ (see Supplementary Fig. S2o and S2p). This S–B ratio is up to 9 times larger than the state-of-the-art free-standing micro-sensors made of carbon fibers (see Supplementary Information Table S2) (Heien et al., 2003; Schmidt et al., 2013; Schwerdt et al., 2018). This remarkable characteristic of NG micro-sensors opens doors for realizing compact and power-efficient detection ICs that are capable of recording the total current (both the background and the redox current) with high precision.

NG micro-sensors are excellent candidates for building lab-on-a-chip systems for imaging chemical activities in complex biological environments (e.g., the brain) with high spatiotemporal resolution. However, a practical difficulty for any electrochemical sensor is the rapid loss of sensitivity in complex biological fluids (such as human serum) due to biofouling. Biofouling has been reported for different sensor materials such as gold and carbon (e.g., see (Nicolai et al., 2017; Puthongkham and Venton 2019; Singh et al., 2011; Vreeland et al., 2015; Weese et al., 2019)). The development of antifouling coatings that work based on size exclusion has become an important and growing field (e.g, see (del Río et al., 2019; Vreeland et al., 2015)). Following similar principles, an important future research direction for deploying NG micro-sensors in complex biological samples is to develop an appropriate antifouling coating.

CRediT authorship contribution statement

Edoardo Cuniberto: Conceptualization, Methodology, Investigation, Formal analysis, Writing - original draft. **Abdullah Alharbi:** Methodology, Investigation, Writing - review & editing. **Zhujun Huang:** Methodology, Investigation, Writing - review & editing. **Ting Wu:** Investigation, Writing - review & editing. **Roozbeh Kiani:** Supervision, Writing - review & editing. **Davood Shahrjerdi:** Conceptualization, Methodology, Investigation, Formal analysis, Supervision, Writing - original draft.

Declaration of competing interest

The authors declare that they have no known competing financial interests or personal relationships that could have appeared to influence the work reported in this paper.

Acknowledgements

The authors acknowledge partial financial support from NSF (1728051) as well as the instrumentation grants from NSF (MRI-1531664) and Gordon and Betty Moore Foundation (GBMF 4838). The authors also acknowledge the Surface Science Facility of CUNY Advanced Science Research Center for the use of the XPS tool. This research used resources of the ASRC Nano-Fabrication Facility of CUNY in New York. This research used resources of the Center for Functional Nanomaterials, which is a U.S. DOE Office of Science Facility, at Brookhaven National Laboratory (BNL) under Contract No. DE-SC0012704. The authors thank K-D. You for his contribution to the development of the CMOS IC described in Ref.(You et al., 2020). The authors thank K. Kisslinger of BNL for helping with TEM specimen preparation and K. Sardashti of NYU for helping with TEM imaging. RK and TW acknowledge support by the Simons Collaboration on the Global Brain (grant 542997), and Pew Scholarship in the Biomedical Sciences. DS acknowledges Prof. J. Uichanco of U Michigan for helpful discussions.

Appendix A. Supplementary data

Supplementary data to this article can be found online at https://doi.org/10.1016/j.bios.2021.112966.

References

Bard AJ, Faulkner LR. 2001. 2:580-632.
Bath, B.D., Michael, D.J., Trafton, B.J., Joseph, J.D., Runnels, P.L., Wightman, R.M., 2000. Anal. Chem. 72, 5994–6002.
Berfield, J.L., Wang, L.C., Reith, M.E., 1999. J. Biol. Chem. 274, 4876–4882.
Berman, D., Deshmukh, S.A., Narayanan, B., Sankaranarayanan, S.K., Yan, Z., Balandin, A.A., Zinovev, A., Rosenmann, D., Sumant, A.V., 2016. Nat. Commun. 7, 1–8.
Biesinger, M.. http://www.xpsfitting.com/.
Bowling, R., Packard, R.T., McCreery, R.L., 1989. Langmuir 5, 683–688.
Cao, Q., Hensley, D.K., Lavrik, N.V., Venton, B.J., 2019. Carbon 155, 250–257.
Chen, J., Han, Y., Kong, X., Deng, X., Park, H.J., Guo, Y., Jin, S., Qi, Z., Lee, Z., Qiao, Z., 2016. Angew. Chem. Int. Ed. 55, 13822–13827.
Chu, C.-H., Sarangadharan, I., Regmi, A., Chen, Y.-W., Hsu, C.-P., Chang, W.-H., Lee, G.-Y., Chyi, J.-I., Chen, C.-C., Shiesh, S.-C., 2017. Sci. Rep. 7, 1–15.
Cuniberto, E., Alharbi, A., Wu, T., Huang, Z., Sardashti, K., You, K.-D., Kisslinger, K., Taniguchi, T., Watanabe, K., Kiani, R., 2020. Sci. Rep. 10, 1–11.
Day, J.J., Roitman, M.F., Wightman, R.M., Carelli, R.M., 2007. Nat. Neurosci. 10, 1020–1028.
del Río, J.S., Henry, O.Y., Jolly, P., Ingber, D.E., 2019. Nat. Nanotechnol. 14, 1143–1149.
Demuru, S., Nela, L., Marchack, N., Holmes, S.J., Farmer, D.B., Tulevski, G.S., Lin, Q., Deligianni, H., 2018. ACS Sens. 3, 799–805.
Dengler, A.K., McCarty, G.S., 2013. J. Electroanal. Chem. 693, 28–33.
Dubey, R., Guruviah, V., 2019. Ionics 25, 1419–1445.
DuVall, S.H., McCreery, R.L., 1999. Anal. Chem. 71, 4594–4602.
DuVall, S.H., McCreery, R.L., 2000. J. Am. Chem. Soc. 122, 6759–6764.
Gerhardt, G.A., Oke, A.F., Nagy, G., Moghaddam, B., Adams, R.N., 1984. Brain Res. 290, 390–395.
Hart, A.S., Rutledge, R.B., Glimcher, P.W., Phillips, P.E., 2014. J. Neurosci. 34, 698–704.
Heien, M.L., Phillips, P.E., Stuber, G.D., Seipel, A.T., Wightman, R.M., 2003. Analyst 128, 1413–1419.
Hirunsit, P., Liangruksa, M., Khanchaitit, P., 2016. Carbon 108, 7–20.
Huffman, M.L., Venton, B.J., 2009. Analyst 134, 18–24.
Ji, H., Zhao, X., Qiao, Z., Jung, J., Zhu, Y., Lu, Y., Zhang, L.L., MacDonald, A.H., Ruoff, R. S., 2014. Nat. Commun. 5, 3317.
Jodko-Piorecka, K., Litwinienko, G., 2013. ACS Chem. Neurosci. 4, 1114–1122.
Millar, J., Stamford, J.A., Kruk, Z.L., Wightman, R.M., 1985. Eur. J. Pharmacol. 109, 341–348.
Mu, L., Chang, Y., Sawtelle, S.D., Wipf, M., Duan, X., Reed, M.A., 2015. IEEE Access 3, 287–302.
Narang, R., Saxena, M., Gupta, M., 2017. Microsyst. Technol. 23, 3149–3159.
Nicolai, E.N., Trevathan, J.K., Ross, E.K., Lujan, J.L., Blaha, C.D., Bennet, K.E., Lee, K.H., Ludwig, K.A., 2017. In: 2017 IEEE International Symposium on Medical Measurements and Applications (MeMeA). IEEE, pp. 111–116.
Pak, A.J., Paek, E., Hwang, G.S., 2014. Carbon 68, 734–741.
Puthongkham, P., Venton, B.J., 2019. ACS Sens. 4, 2403–2411.
Rice, R.J., McCreery, R.L., 1989. Anal. Chem. 61, 1637–1641.
Rodeberg, N.T., Sandberg, S.G., Johnson, J.A., Phillips, P.E., Wightman, R.M., 2017. ACS Chem. Neurosci. 8, 221–234.
Runnels, P.L., Joseph, J.D., Logman, M.J., Wightman, R.M., 1999. Anal. Chem. 71, 2782–2789.
Sambrook J, Fritsch EF, Maniatis T. 1989. Cold spring harbor laboratory press, Cold Spring Harbor, New York, volume 3, apendix B.12.
Schmidt, A.C., Wang, X., Zhu, Y., Sombers, L.A., 2013. ACS Nano 7, 7864–7873.
Schwerdt, H.N., Zhang, E., Kim, M.J., Yoshida, T., Stanwicks, L., Amemori, S., Dagdeviren, H.E., Langer, R., Cima, M.J., Graybiel, A.M., 2018. Commun. Biol. 1, 1–11.
Singh, Y.S., Sawarynski, L.E., Dabiri, P.D., Choi, W.R., Andrews, A.M., 2011. Anal. Chem. 83, 6658–6666.
Sugam, J.A., Day, J.J., Wightman, R.M., Carelli, R.M., 2012. Biol. Psychiatr. 71, 199–205.

Takmakov, P., Zachek, M.K., Keithley, R.B., Bucher, E.S., McCarty, G.S., Wightman, R.M., 2010. Anal. Chem. 82, 9892–9900.
Venton, B.J., Cao, Q., 2020. Analyst 145, 1158–1168.
Villanueva, J.T., Huang, Q., Fischer, N.O., Arya, G., Sirbuly, D.J., 2018. J. Phys. Chem. C 122, 22114–22124.
Vreeland, R.F., Atcherley, C.W., Russell, W.S., Xie, J.Y., Lu, D., Laude, N.D., Porreca, F., Heien, M.L., 2015. Anal. Chem. 87, 2600–2607.
Weese, M.E., Krevh, R.A., Li, Y., Alvarez, N.T., Ross, A.E., 2019. ACS Sens. 4, 1001–1007.
Wightman, R.M., 1981. Anal. Chem. 53, 1125A–1134A.
Wu, T., Alharbi, A., Kiani, R., Shahrjerdi, D., 2019. Adv. Mater. 31, 1805752.
Yang, C., Trikantzopoulos, E., Nguyen, M.D., Jacobs, C.B., Wang, Y., Mahjouri-Samani, M., 2016. Ivanov IN, Venton BJ. ACS Sens. 1, 508–515.
You, K.-D., Cuniberto, E., Hsu, S.-C., Wu, B., Huang, Z., Pei, X., Shahrjerdi, D., 2020. In: IEEE Transactions on Biomedical Circuits and Systems, 14, pp. 903–917.
Zhong, J.-H., Zhang, J., Jin, X., Liu, J.-Y., Li, Q., Li, M.-H., Cai, W., Wu, D.-Y., Zhan, D., Ren, B., 2014. J. Am. Chem. Soc. 136, 16609–16617.
Zhu, Z., 2017. Nano-Micro Lett. 9, 25.

Supplementary Information

Anomalous sensitivity enhancement of nano-graphitic electrochemical micro-sensors with reducing the operating voltage

Edoardo Cuniberto,[1] Abdullah Alharbi,[1,2] Zhujun Huang,[1] Ting Wu,[3] Roozbeh Kiani,[3,4] Davood Shahrjerdi[1,5]*

[1] Electrical and Computer Engineering, New York University, Brooklyn, NY 11201,

[2] National Center for Nanotechnology and Semiconductors, KACST, Riyadh, Saudi Arabia 11442,

[3] Center for Neural Science, New York University, New York, NY, 10003,

[4] Department of Psychology, New York University, New York, NY 10003,

[5] Center for Quantum Phenomena, Physics Department, New York University, New York, NY 10003,

* E-mail: davood@nyu.edu

S1. Synthesis of nano-graphitic carbon material

The synthesis of nano-graphitic (NG) carbon followed the same steps described in our previous study [1]. Specifically, the synthesis started with patterning micron-size SU8 islands directly on SiO_2 substrates using electron-beam lithography (EBL). The SU8 islands were then converted into a fully sp^2 carbon through a carbonization step by annealing the samples at 450 °C in a non-oxidizing ambient (80/20 mixture of Ar/H_2). Lastly, the solid-state transformation of the amorphous carbon island into NG carbon involved the deposition of an ultra-thin nickel layer (<1 nm) in ultra-high vacuum (base pressure of $\sim 1\times10^{-10}$ mbar) followed by annealing at 1100 °C in a Ar/H_2 (80/20 mixture).

S2. Atomic composition and chemistry of NG micro-sensor surface

We used x-ray photo-electron spectroscopy (XPS) to study the atomic and chemical composition of the sensor surface. Fig. S1a shows the x-ray induced secondary electron image (SXI) of a micro-sensor. We used this image to adjust the location of the x-ray beam for XPS measurements (the red cross). We note that the x-ray spot size in these experiments was comparable to the size of the micro-sensor. As a result, the x-ray beam in our experiments was impinging both on the micro-sensor and on the SiO_2

substrate. This is obvious from the full-survey XPS scan in Fig. S1b, where there exists noticeable carbon (C 1s) and silicon (Si 2s and Si 2p) peaks.

Next, we analyzed the detailed XPS peaks of each element that are observable in the full-survey scan. The analysis of the carbon C 1s peak (Fig. S1c) indicates that the NG micro-sensor surface consists of sp^2-hybridized C-C bonds. This is evident from both the position and the asymmetry of the C 1s peak. This observation is consistent with the fully capacitive nature of the background current of the NG micro-sensors.

The detailed scan for the primary XPS region of Ni (Fig. S1d) showed no detectable Ni on the sensor surface. The analysis of the oxygen O 1s peak (Fig. S1e) indicates that the primary origin of this peak is SiO_2. For this analysis, we considered two Gaussian peaks: one oxygen peak for SiO_2, located at 532.9 eV, and another oxygen peak for the carbonates, located at around 531.3 eV [2]. As shown in Fig. S1e, the single oxygen peak of SiO_2 provides an excellent fit to the collected O 1s data, indicating no detectable carbonates on the surface of the NG micro-sensor. Finally, the detailed scan of the silicon Si 2p peak confirms that the x-ray beam extends beyond the micro-sensor and over the SiO_2 substrate in our XPS measurements.

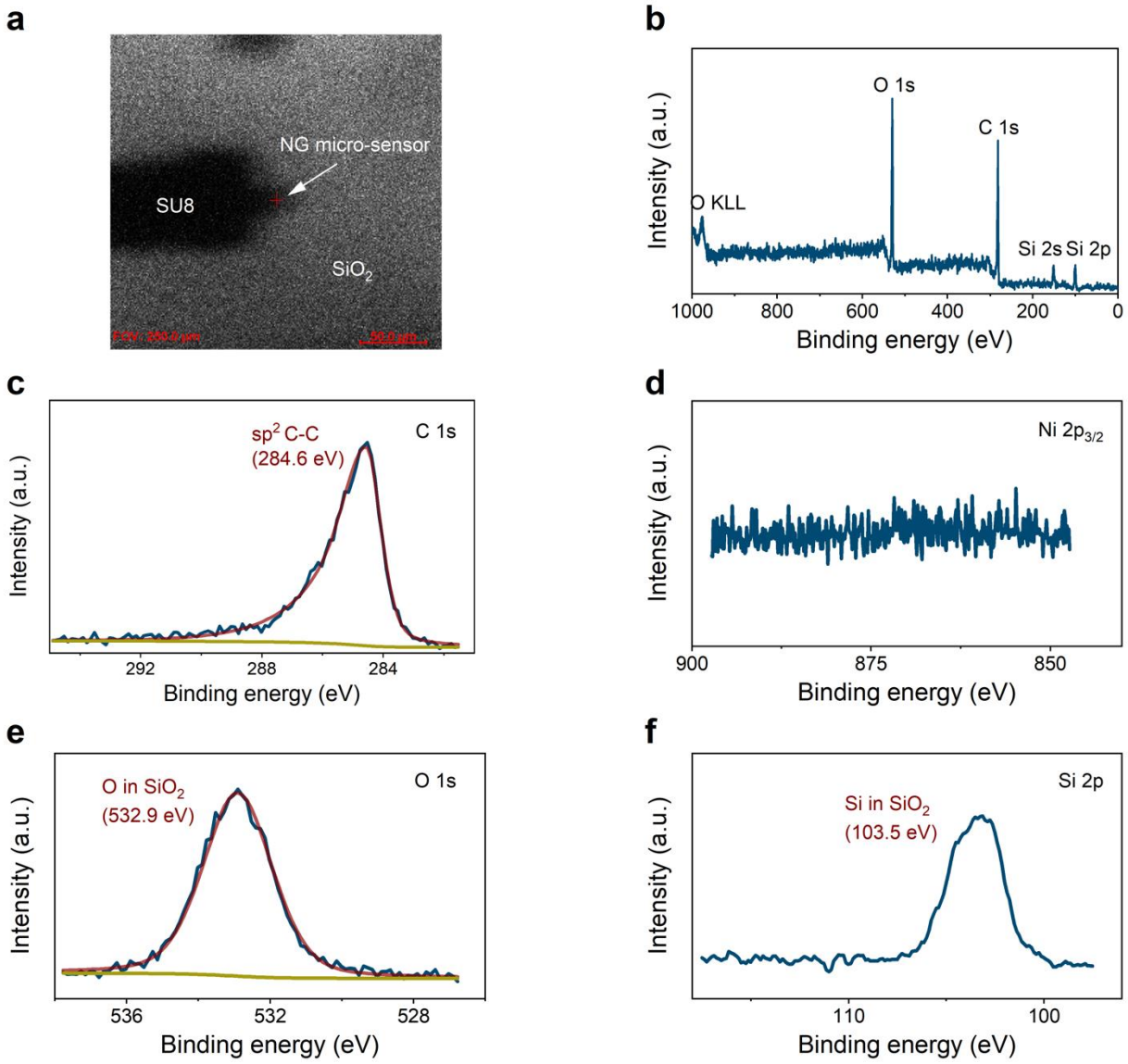

Figure S1: a) X-ray induced secondary-electron image of a NG micro-sensor used for XPS studies. **b)** The full-survey XPS scan showing noticeable Si 2p, Si 2s, C 1s, O 1s and O KLL peaks. **c)** Detailed carbon C 1s peak. **d)** Detailed scan of primary XPS region of Ni. **e)** Detailed oxygen O 1s peak. **f)** Detailed silicon Si 2p peak.

S3. Multi-physics numerical simulation

The simulations were carried out in COMSOL Multiphysics. In our simulations, we used a multi-physics model including electrostatic and ionic transport. To model the distribution of ions at the electrode/electrolyte solution, we used the Stern model. This model is a combination of two classical theories proposed by Helmholtz and Gouy-Chapman. Briefly, the Stern model states that the charge density on the electrode is balanced by a Helmholtz layer as well as a diffusive layer extending into the bulk. Therefore, in our simulation, we divided the electrolyte in two parts: a Helmholtz layer and a diffusive layer.

We approximated the thickness of the Helmholtz layer by calculating the Debye length of the electrolyte, where the Debye length is given by

$$k^{-1} = \sqrt{\frac{\varepsilon_r \varepsilon_0 \, k_B T}{2 c_0 \, z^2 e^2}}$$

In this equation, ε_0 is the permittivity of free space, ε_r is the dielectric constant of 1X PBS (we assumed it to be 80), k_B is the Boltzmann constant, T is the absolute temperature (300 K in our case), c_0 is the bulk electrolyte concentration (around 160 mM in 1X PBS), z^2 is the ionic charge (we assumed it to be 1) and *e* is the elementary charge. By plugging these values into the above equation, we obtained a Debye length (k^{-1}) of ≈0.75 nm.

S4. UPL dependence measurement results of our NG micro-sensors

We tested the generalizability of the UPL dependence phenomenon on NG micro-sensors, which were fabricated in different runs and under different processing conditions. Specifically, those sensors were produced by only varying the nickel thickness between 0.5 nm to 1 nm during the NG carbon synthesis. Fig. S2 shows the background current and the cyclic voltammogram of eight micro-sensors. Notice that the shape and the amplitude of the background current of these sensors do not change by varying UPL. In contrast, $I_{ox,peak}$ of all sensors shows strong dependence on UPL—that is, it increases with decreasing UPL. These observations indicate that the UPL-induced enhancement of the sensitivity is universal to the NG micro-sensors.

The above characteristics of the NG micro-sensors result in the increase of the sensitivity relative to the background charging current (I_{bg}) by decreasing UPL. Specifically, we refer to the ratio of $I_{ox,peak}$ at 1 μM of dopamine to I_{bg} as the S-B ratio. Table S1 summarizes the S-B ratio of the eight NG micro-sensors, which are shown in Fig. S2.

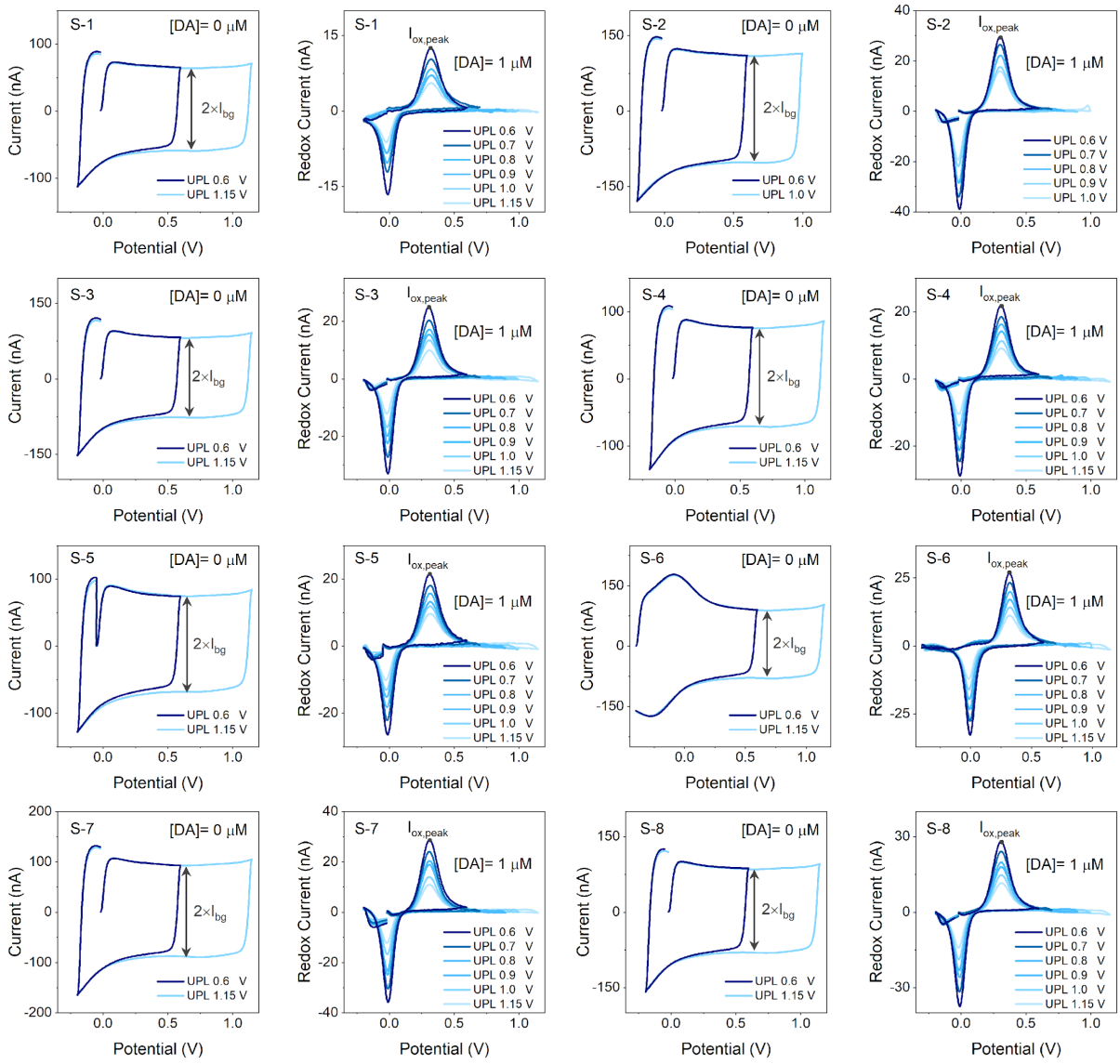

Figure S2: The UPL dependence characteristics of the background currents as well as the cyclic voltammograms of eight NG micro-sensors.

Table S1. NG micro-sensors characteristics.

Sensor ID	I_{bg} (nA)	$I_{ox,peak}$ (nA) UPL=0.6 V, [DA]=1 µM	S-B ratio ($nA.\mu M^{-1}.nA^{-1}$)
S-1	60	12.5	0.21
S-2	106	29.6	0.28
S-3	79	24.9	0.31
S-4	68	21.8	0.32
S-5	67	21.6	0.32
S-6	80	26.8	0.33
S-7	85	28.7	0.34
S-8	80	28.2	0.35

S5. Effect of the reaction chamber geometry

We investigated whether the geometry of the reaction chamber influences the UPL dependence of the oxidation current by substituting the Y-shaped chamber with a cylindrical one. Fig. S3a shows the experimental setup with the cylindrical chamber. In these experiments, we performed the voltammetry measurements using the RPS waveform identical to those used for the experiments carried out with the Y-shaped chamber (i.e., N-shaped waveform, ν=200 V/s, LPL=-0.2 V, varying UPL ranging from 0.6 V to 1.15 V). The concentration of dopamine solution in these experiments was 500 nM.

Fig. S3b shows the corresponding cyclic voltammograms obtained from these measurements. The results show that the amplitude of the redox current is a strong function of UPL. In Fig. S3c, we show the summary plot of the normalized peak oxidation current ($I_{ox,peak}$) against UPL. The data points labeled “Cylindrical” were obtained from the voltammograms in Fig. S3b. The new data obtained using the cylindrical chamber follow the same linear trend as those obtained using the Y-shaped microfluidic chamber. This result shows that the geometry of the reaction chamber does not have a noticeable effect on the observed UPL dependence of the oxidation current.

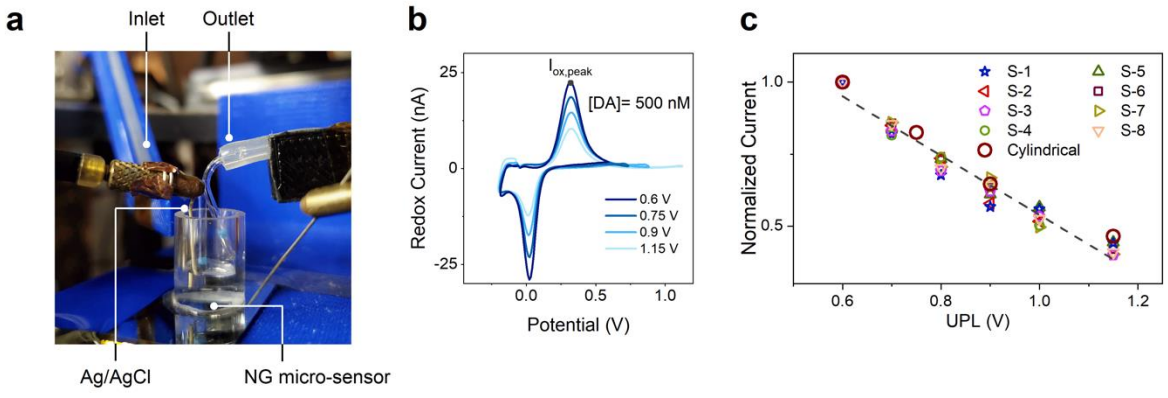

Figure S3: a) Photo of the experimental setup, showing the cylindrical reaction chamber. **b)** Dopamine cyclic voltammograms obtained from the experiments using the cylindrical reaction chamber. The data indicate that the sensitivity increases by decreasing UPL. **c)** Normalized $I_{ox,peak}$ plotted against UPL for multiple NG micro-sensors. The UPL dependence for the measurements using the cylindrical reaction chamber is consistent with those performed using the Y-shaped chamber.

S6. Low-concentration measurements of dopamine

Fig. S4 shows additional measurements for the detection of dopamine at low concentrations. These measurements were performed using a read-out circuit made of commercial off-the-shelf (COTS) components. Figs. S4a-b show the cyclic voltammograms of dopamine for concentrations ranging from 500 nM to 10 nM. The measurements were performed using an N-shaped waveform with a sweep rate of 400 V/s. The LPL and UPL of the N-shaped waveform were -0.3 V and 0.75 V. Fig. S4c shows the corresponding calibration curve, confirming the well-behaved characteristics of our NG sensors. Fig. S4d shows the redox currents of dopamine measured at 10 and 20 nM plotted against time. The ability to measure low concentrations of dopamine is a direct consequence of the high S-B ratio of our sensors.

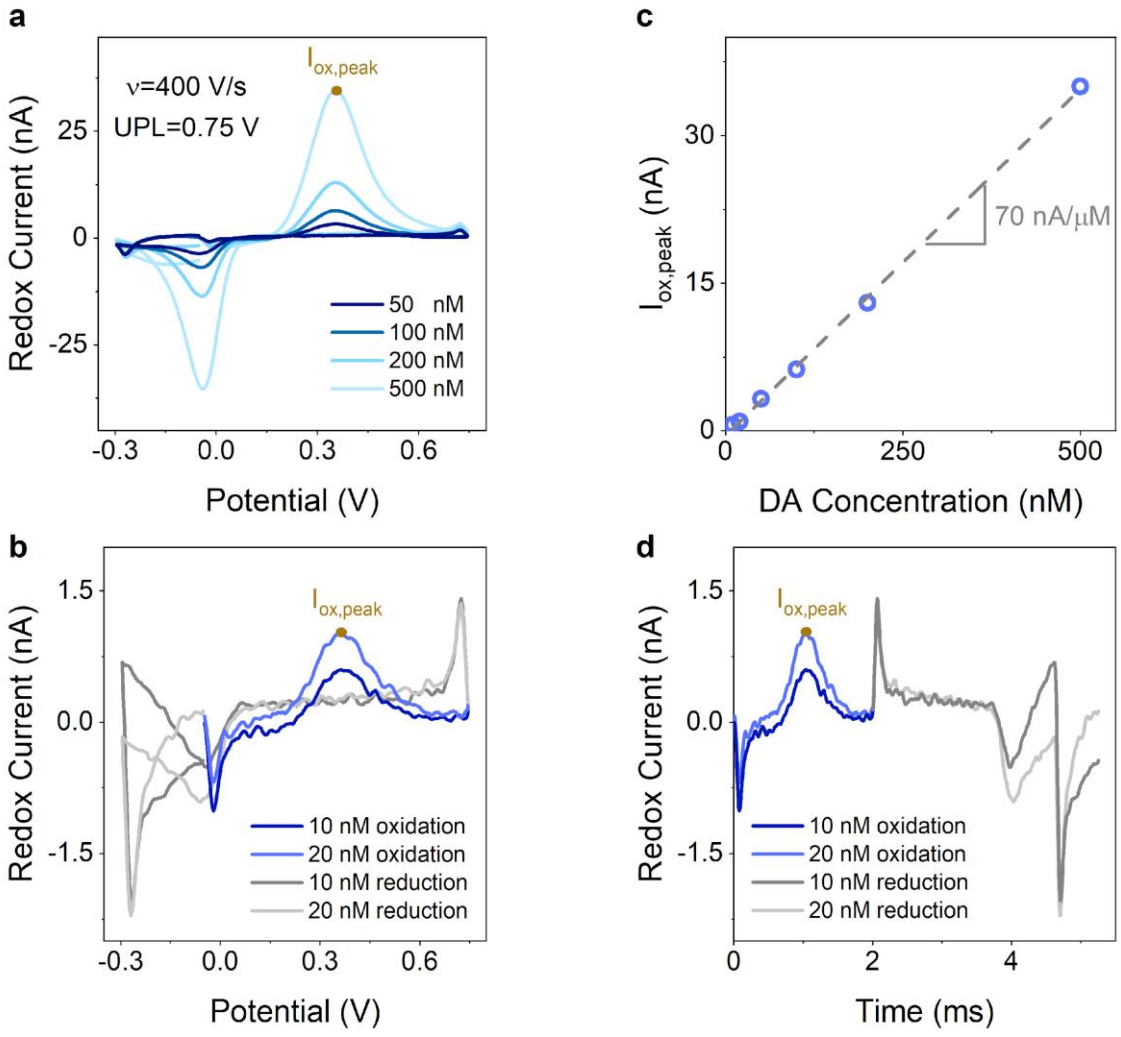

Figure S4: a) Measured cyclic voltammograms of dopamine for concentrations ranging from 50 nM to 500 nM. **b)** Measured cyclic voltammograms of dopamine for 10 nM and 20 nM. **c)** Calibration curve showing the linearity of the NG micro-sensor. The linear fit to the data gives a sensitivity of 70 nA/μM. **d)** Redox current of low-concentration dopamine plotted against time.

S7. The quality of calibration curves

Fig. S5a-b show the calibration curves for two NG carbon micro-sensors along with the 95% confidence bands of the linear fits (the red bands). Notice that all data points are well within the confidence bands, indicating the excellent linear behavior of our micro-sensors for the measured range of dopamine in the calibration curve. Further, the calibration curves have a negligible offset (i.e., the intercept with the y-axis). This characteristic is critical for a reliable interpretation of sensing measurement data using the calibration curves.

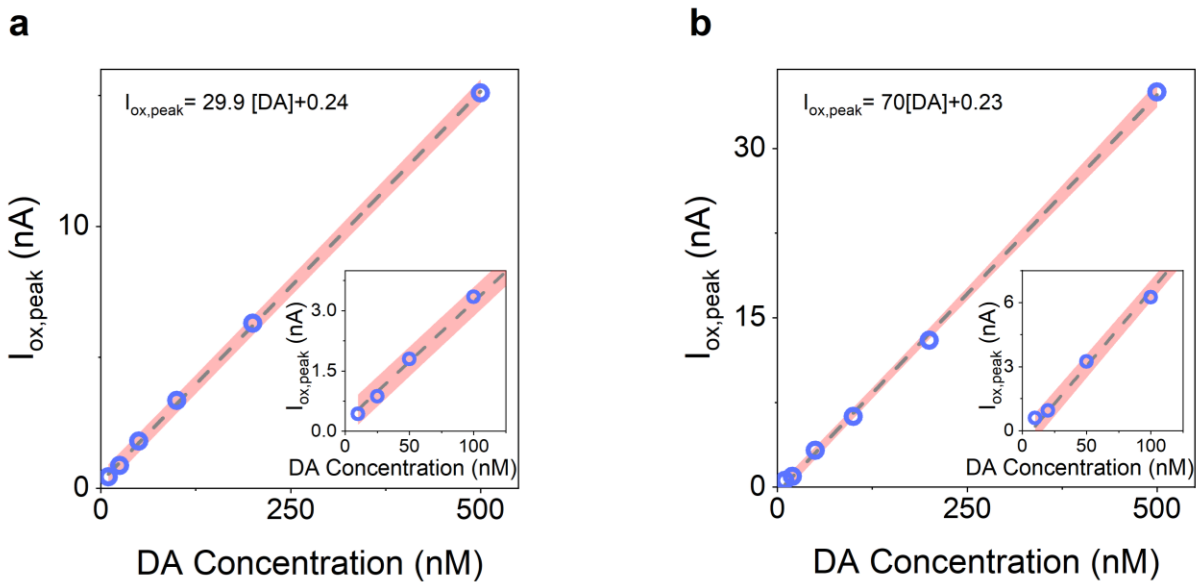

Figure S5: Calibration curves for two NG micro-sensors. The curve fitting results confirm the well-behaved characteristics of the NG micro-sensors. The DA concentration ([DA]) is in units of μM.

S8. S-B ratio comparison with other carbon micro-sensors

Table S2 shows the summary of the sensitivity-to-background (S-B) ratio for a few representative state-of-the-art carbon micro-sensors.

Table S2. S-B ratio comparison of NG micro-sensors with other carbon micro-sensors. For references [3,4,6,7], we estimated the S-B ratio by taking the ratio of the oxidation current measured at 1 μM dopamine to the background current.

Material	S-B ratio ($nA.\mu M^{-1}.nA^{-1}$)	Reference
NG micro-sensor	0.35	This work
Carbon fiber (P-55)	~0.01	[3]
Carbon fiber (T-650)	~0.04	[4]
μIP carbon fiber	~0.04-0.08	[5]
Carbon nanotube yarn	~0.1	[4]
Carbon nanospikes	~0.03	[6]
Nanodiamond coating	~0.07	[7]

References

[1] E. Cuniberto, A. Alharbi, T. Wu, Z. Huang, K. Sardashti, K.-D. You, K. Kisslinger, T. Taniguchi, K. Watanabe, R. Kiani, Nano-engineering the material structure of preferentially oriented nano-graphitic carbon for making high-performance electrochemical micro-sensors, Scientific Reports 10(1) (2020) 1-11.
[2] M. Biesinger. http://www.xpsfitting.com/.
[3] J.A. Johnson, N.T. Rodeberg, R.M. Wightman, Measurement of basal neurotransmitter levels using convolution-based nonfaradaic current removal, Analytical chemistry 90(12) (2018) 7181-7189.
[4] A.C. Schmidt, X. Wang, Y. Zhu, L.A. Sombers, Carbon nanotube yarn electrodes for enhanced detection of neurotransmitter dynamics in live brain tissue, Acs Nano 7(9) (2013) 7864-7873.
[5] H.N. Schwerdt, E. Zhang, M.J. Kim, T. Yoshida, L. Stanwicks, S. Amemori, H.E. Dagdeviren, R. Langer, M.J. Cima, A.M. Graybiel, Cellular-scale probes enable stable chronic subsecond monitoring of dopamine neurochemicals in a rodent model, Communications biology 1(1) (2018) 1-11.
[6] Q. Cao, D.K. Hensley, N.V. Lavrik, B.J. Venton, Carbon nanospikes have better electrochemical properties than carbon nanotubes due to greater surface roughness and defect sites, Carbon 155 (2019) 250-257.
[7] P. Puthongkham, B.J. Venton, Nanodiamond coating improves the sensitivity and antifouling properties of carbon fiber microelectrodes, ACS sensors 4(9) (2019) 2403-2411.